Title
A Dual-Ion Battery Cathode via Oxidative Insertion of Anions in a Metal-Organic Framework.

Journal
Journal of the American Chemical Society, 137(42)

ISSN
0002-7863

Authors
Aubrey, Michael L
Long, Jeffrey R

Publication Date
2015-10-01

DOI
10.1021/jacs.5b08022

Peer reviewed

JACS
JOURNAL OF THE AMERICAN CHEMICAL SOCIETY

Article

pubs.acs.org/JACS

A Dual–Ion Battery Cathode via Oxidative Insertion of Anions in a Metal–Organic Framework

Michael L. Aubrey[†,‡] and Jeffrey R. Long*[,†,‡]

[†]Department of Chemistry, University of California, Berkeley, California 94720, United States

[‡]Materials Sciences Division, Lawrence Berkeley National Laboratory, Berkeley, California 94720, United States

Supporting Information

ABSTRACT: A redox–active metal–organic framework, Fe_2(dobpdc) (dobpdc^{4-} = 4,4′-dioxidobiphenyl-3,3′-dicarboxylate), is shown to undergo a topotactic oxidative insertion reaction with a variety of weakly coordinating anions, including BF_4^- and PF_6^-. The reaction results in just a minor lattice contraction, and a broad intervalence charge-transfer band emerges, indicative of charge mobility. Although both metal- and ligand-based oxidations can be accessed, only the former were found to be fully reversible and, importantly, proceed stoichiometrically under both chemical and electrochemical conditions. Electrochemical measurements probing the effects of nanoconfinement on the insertion reaction revealed strong anion size and solvent dependences. Significantly, the anion insertion behavior of Fe_2(dobpdc) enabled its use in the construction of a dual-ion battery prototype incorporating a sodium anode. As a cathode, the material displays a particularly high initial reduction potential and is further stable for at least 50 charge/discharge cycles, exhibiting a maximum specific energy of 316 Wh/kg.

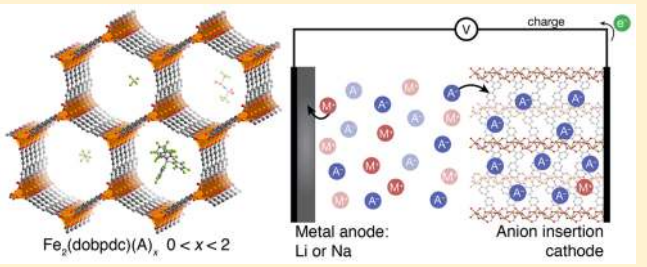

1. INTRODUCTION

Underpinning a vast number of advanced materials, the intercalation reaction, a slipping of an ion or molecule through the galleries of a 2D host lattice, and its more general 3D analogue, the insertion reaction, allow the electronic properties of a host lattice to be dramatically altered.[1] In particular, reductive insertion has revolutionized rechargeable batteries. The general reaction mechanism is a simple one: a material with weakly interacting sheets, interconnected site vacancies, or tunnels accommodates a metal cation while a charge-balancing electron is transferred to the host lattice via a circuit.

Although insertion reactions are well-established for a plethora of metal cations, it is remarkably challenging to accomplish the same task with negative ions.[2] This difficulty is because electrochemically stable anions are large compared to metal cations; hence, their accommodation requires a much greater accessible volume. Indeed, inorganic materials that reversibly intercalate anions are rare, with the hydrotalcite structure type and graphite intercalation compounds largely making up the class.[3−7] These materials are layered compounds with sheets that are easily separated. As such, the distance between the layers can increase to accommodate large guest species. In contrast, the implicit rigidity of a 3D host lattice culminates in a dearth of topotactic anion insertion materials.

Of particular interest with respect to energy storage is the possible insertion of anions stable at strongly oxidizing potentials, such as tetrafluoroborate (BF_4^-), hexafluorophosphate (PF_6^-), and bis(trifluoromethylsulfonyl)imide ($TFSI^-$). Unfortunately, the large ionic radii of these weakly coordinating anions necessitate substantial changes in the unit cell volume of the electrode material upon oxidative insertion. For graphite, 15, 16, and 20% increases in cell volume were observed upon intercalation of BF_4^-, PF_6^-, and $TFSI^-$, respectively.[8] Certain conducting organic polymers can not only be reversibly oxidized through a similar mechanism but also swell substantially upon insertion.[9] In fact, this swelling phenomenon is of such sufficient magnitude that it has been leveraged to construct electrochemical actuators.[10,11]

Metal–organic frameworks are hybrid materials with permanently porous structures that can be modified in a building blocklike fashion.[12,13] Because of the large pore sizes, they are also highly amenable to postsynthetic modification, which often requires the accommodation of large guest molecules.[14,15] Over the past few years, the number of metal–organic framework semiconductors has increased rapidly.[16−19] Recently, it was shown that by selecting a framework structure with infinite chains of redox-active vanadium(IV) or iron(III) centers, a mixed-valence state could be engendered via reduction, thereby mediating electron diffusion, whereas the large pores facilitate concomitant cation insertion.[20−23] However, the specific energies reported in these previous studies were generally low or the materials were not found to be phase stable.[24−26] At a glance, this is to be expected, given the size of the inert organic linkers that do not contribute to the total charge capacity of the material. In

Received: August 6, 2015

DOI: 10.1021/jacs.5b08022
J. Am. Chem. Soc. XXXX, XXX, XXX–XXX

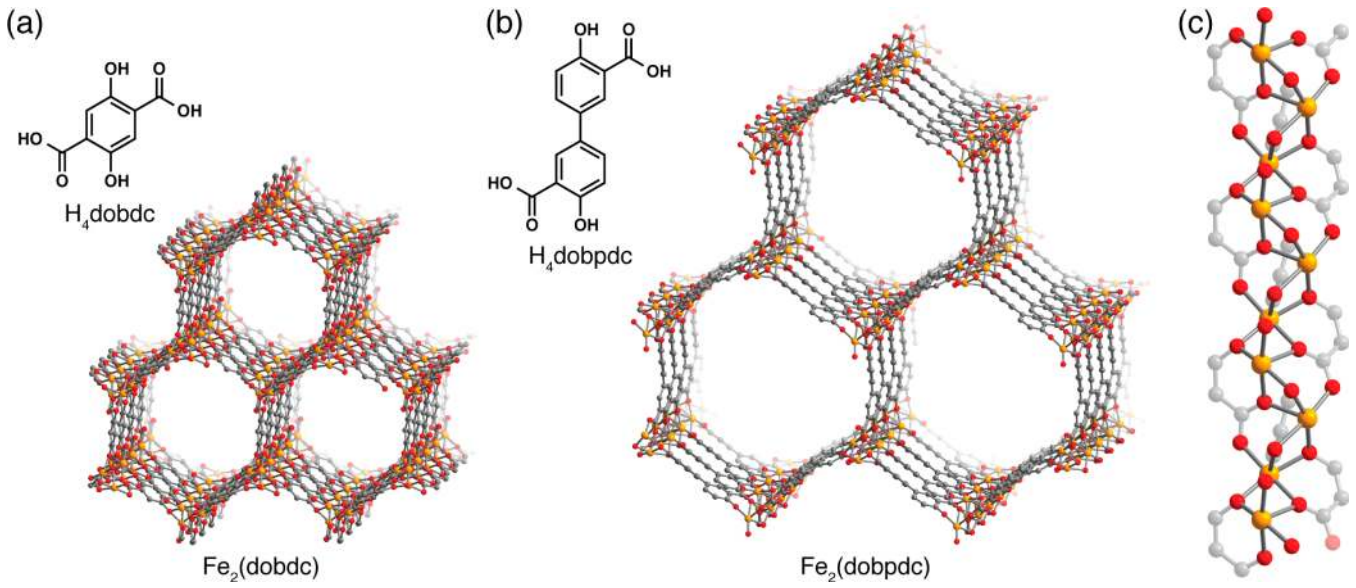

Figure 1. Structure of the framework (a) Fe_2(dobdc) and (b) Fe_2(dobpdc). (c) The structures are isoreticular and crystallize in a trigonal lattice with edge-sharing Fe(II) chains running parallel to the *c* axis. The desolvated structure is shown here for clarity. The pseudosquare pyramidal iron centers retain an open coordination site that points toward the center of the hexagonal pore. The longest distance across the channel for Fe_2(dobdc) is 12 Å, and for Fe_2(dobpdc), it is 21 Å.

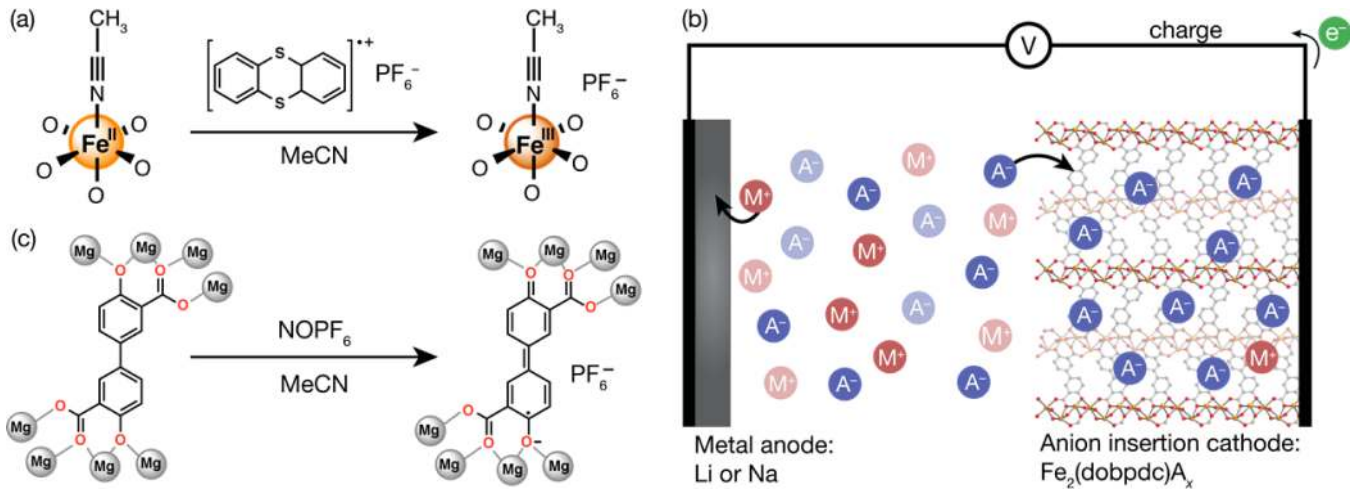

Figure 2. (a) Reaction scheme for postsynthetic oxidation of Fe_2(dobpdc). Oxidation with thianthrenium hexafluorophosphate was carried out in acetonitrile. (b) Generalized schematic of how Fe_2(dobpdc) operates in an electrochemical cell and (c) postsynthetic oxidation of the isostructural Mg_2(dobpdc) with nitrosonium hexafluorophosphate to yield an organic radical. For the electrochemical reduction in b anions, A^-, can be tetrafluoroborate, hexafluorophosphate, bis(trifluoromethylsulfonyl)imide, or tetrakis(perfluorophenyl)borate and cations, M^+, can be lithium, sodium, or potassium.

concert with the intrinsically low energy densities of porous electrodes, metal−organic frameworks have not yet proven promising as competitive battery electrodes. However, to our knowledge, the possible oxidative insertion of anions has not yet been investigated for this class of materials. Here, we demonstrate the efficacy of selected redox-active metal−organic frameworks for undergoing reversible anion insertion reactions with a high specific energy and utilize this capability in the construction of a dual-ion battery half-cell prototype.

2. RESULTS AND DISCUSSION

At least conceptually, it seems straightforward to design a metal−organic framework for an electrochemical anion insertion reaction. Toward this end, we sought a rigid 3D framework with pores large enough to accommodate large ions; this encompasses the bulk of the metal−organic frameworks reported. What is rare yet most important, however, is a structural motif with short distances between redox-active metal centers that extends uninterrupted through the crystal. Because these metal centers contribute significantly to the valence band of the framework, judicious selection of a reversible redox manifold yields both a mode of charge storage and potentially substantial gains in electronic conductivity.[27] Lastly, the low gravimetric densities of redox sites must be addressed. The two most obvious solutions are to increase linker topicity, and therefore the metal to linker ratio, and to install structural motifs on the ligands that also reversibly store charge.

With this in mind, one metal−organic framework in particular, Fe_2(dobdc), ($dobdc^{4-}$ = 2,5-dioxidobenzene-1,4-dicarboxylate), presented itself. Materials of this type are

DOI: 10.1021/jacs.5b08022
J. Am. Chem. Soc. XXXX, XXX, XXX−XXX

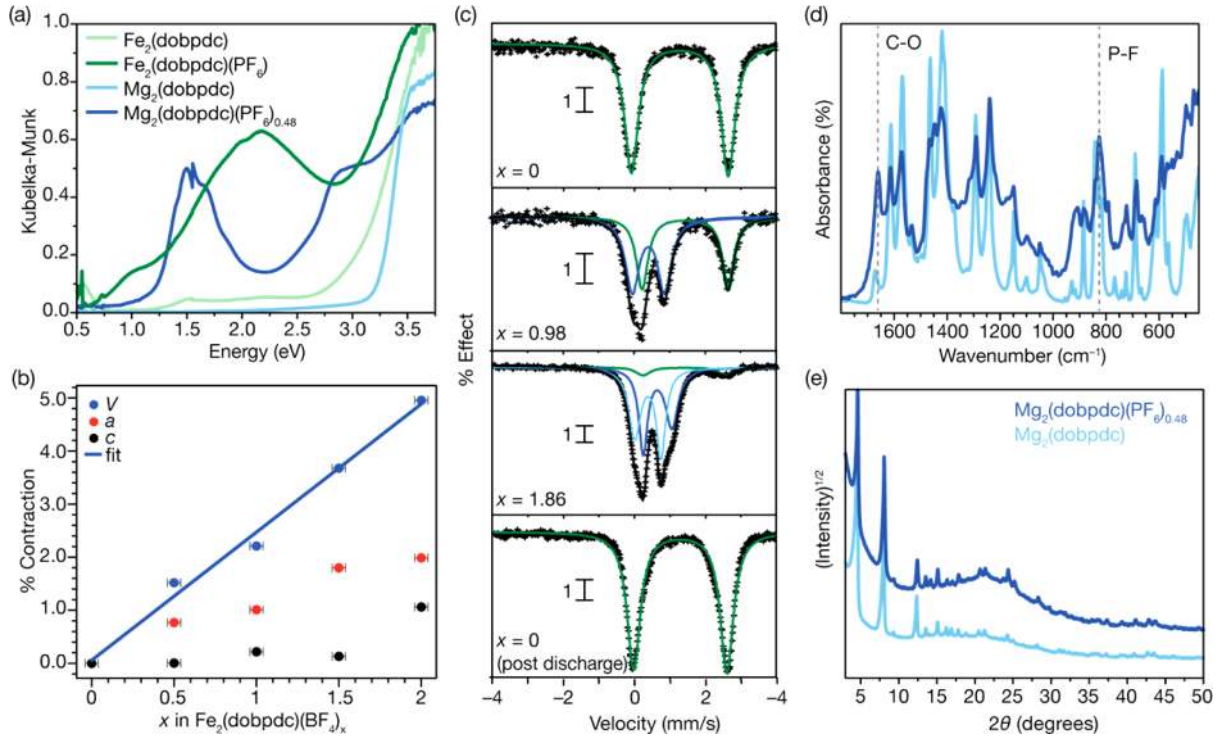

Figure 3. (a) NIR–vis–UV absorption spectrum for chemically oxidized samples, (b) unit cell parameters determined ex situ powder X-ray diffraction for electrochemically oxidized samples of $Fe_2(dobpdc)(BF_4)_x$, and (c) ex situ ^{57}Fe Mössbauer spectra for electrochemically oxidized samples of $Fe_2(dobpdc)(BF_4)_x$, experimental data (+), high-spin iron(II) (green), high-spin iron(III) (blue and light blue), and the fits (black). The values of x in b and c correspond to $Fe_2(dobpdc)(BF_4)_x$ and were determined electrochemically. Samples were oxidized in three electrode electrochemical cells with lithium counter and reference electrodes and a 0.1 M $LiBF_4$ electrolyte in propylene carbonate. (d) Infrared spectra of $Mg_2(dobpdc)$ (light blue) and $Mg_2(dobpdc)(PF_6)_{0.48}$ (dark blue) revealed a new C–O stretch (1661 cm^{-1}) and a new P–F stretch (823 cm^{-1}) after oxidation. (e) Powder X-ray diffraction of $Mg_2(dobpdc)$ (light blue) and $Mg_2(dobpdc)(PF_6)_{0.48}$ (dark blue) show a 0.9% contraction in unit cell. The very broad feature at 20° originates from the borosilicate glass capillary used to exclude air from the sample.

noteworthy for their remarkable gas sorption properties owing to their high density of gas–accessible binding sites at the metal ions.[28−32] $Fe_2(dobdc)$ is attractive from the molecular formula alone; its molar mass per metal ion is 57% greater than the similarly structured metal–organic-framework-based lithium-insertion material Fe(1,4-benzenedicarboxylate) $(OH)_{0.8}(F)_{0.2}$ and near identical to $FePO_4$.[21] The framework, shown in Figure 1a, has hexagonal channels with five-coordinate Fe^{2+} ions lining the vertices in infinite 1D chains of edge-sharing square pyramids.[28] When solvated, the iron centers are pseudo-octahedral. Similar phases are known to be redox-active and semiconducting.[33,34] Because this material contains iron(II), unlike other iron insertion compounds, it must insert anions in order to access the $Fe^{II/III}$ couple.

By chemical oxidation with thianthrenium hexafluorophosphate (Figure 2a), a stoichiometric oxidation to the half-ferric phase $Fe_2(dobdc)(PF_6)_{0.96}{\cdot}y$MeCN ($y \approx 2.6$) was obtainable at room temperature. This stoichiometry was confirmed by ^{57}Fe Mössbauer spectroscopy and is further supported by a small contraction of the unit cell, which results from the smaller radius of the Fe^{3+} ion (Figures S1 and S2). Attempts at electrochemical oxidation were carried out, but only a much smaller fraction of the iron sites could be oxidized (Figure S3). Such a strong dependence on the reaction solvent results from solvent coordination to the iron sites, as discussed below. Nonetheless, the oxidation of $Fe_2(dobdc)$ represents, to the best of our knowledge, the first topotactic oxidative insertion of a noncoordinating anion and an exceptionally rare case of negative volume expansion upon topotactic oxidative insertion or epitaxic intercalation.

2.1. Chemical Oxidation of $Fe_2(dobpdc)$. One convenient property of the $M_2(dobdc)$ family is that the pore aperture can be systematically expanded with conservation of network topology and without the possibility of interpenetration.[35] Figure 1b shows one such framework constructed with the larger linker, 4,4′-dioxidobiphenyl-3,3′-dicarboxylate = $dobpdc^{4-}$, with the formula $Fe_2(dobpdc)$. This framework was synthesized previously in our laboratory.[36] With a crystallographic pore diameter ~50% larger than that of $Fe_2(dobdc)$, even with solvent coordinated to the iron sites, a substantial void space remains at the center of the pore.

Chemically, it was found that this phase could be oxidized to $Fe_2(dobpdc)(PF_6)_{1.56}{\cdot}y$MeCN ($y \approx 5.1$) with two equivalents of thianthrenium hexafluorophosphate in acetonitrile (Figure 2a). The resulting material is electrochromic, with the color changing from pale green to a very dark blue upon partial oxidation. As depicted in Figure 3a, the diffuse reflectance UV–vis–NIR spectrum shows this as an appearance of a broad absorption band centered at 2.26 eV and extending down to 0.59 eV, indicative of a Robin–Day Class-II mixed-valence state.[37] This is in contrast to the all-ferrous starting material that only displayed weak d–d transitions and a ligand-centered transition above 2.93 eV.

Infinite chains of edge-sharing octahedra are a prevalent structural motif in mixed-valence iron minerals that display Class-II or Class-III behavior.[38] The nearest Fe···Fe distance of 3.04 Å in $Fe_2(dobdc)$,[28] which should match that in the

DOI: 10.1021/jacs.5b08022
J. Am. Chem. Soc. XXXX, XXX, XXX–XXX

isostructural Fe_2(dobpdc), is the shortest of any metal−organic framework with infinite iron chains. Those that are the next closest are Fe^{III}(gallate)·$2H_2O$ and Fe(bdc)$(OH)_{0.8}(F)_{0.2}$, possessing vertex-sharing octahedra.[21,39]

Powder X-ray diffraction experiments confirmed a topotactic insertion and linear contraction of the unit cell with increasing oxidation, as shown in Figure S12 and Table S4. No new peaks or large changes in intensity were observed upon oxidation. The relative change in unit cell volume was just ∼5% and can be attributed to the smaller ionic radius of Fe^{3+} compared to that of Fe^{2+}. The results suggest a random distribution of iron(II) and iron(III) centers in the host lattice upon oxidation and, similarly, a lack of order for the positions of the PF_6^- counterions within the channels. This leads us to suspect that the coordination environment at all of the iron sites is close to identical.

Iron-57 Mössbauer spectra collected at 100 K are consistent with discrete valencies for the iron sites within Fe_2(dobpdc)-$(PF_6)_x$ (Figure S4). The spectrum of the initial all-ferrous compound, Fe_2(dobpdc), exhibits a single doublet with an isomer shift of δ = 1.297 mm/s and a quadrupole splitting of Δ_E = 2.725 mm/s, consistent with the presence of just one type of high-spin iron(II) center. Upon oxidation to the half-ferric material (x = 1) a new doublet emerges, with δ = 0.372 mm/s and Δ_E = 0.954 mm/s, matching those values expected for a high-spin iron(III) center. The relative area of this new doublet corresponds to the quantity of oxidant that was employed in the oxidation reaction, within mass error. Oxidation to x = 2 was attempted but did not go to completion, with 22% of the metal centers remaining as iron(II). As discussed below, this is likely because the oxidation potential of thianthrenium in acetonitrile is not high enough to achieve full oxidation. Unlike other compounds featuring edge-sharing mixed-valence iron oxide, no significant electron delocalization was detected by variable temperature Mössbauer spectroscopy experiments.[38]

2.2. Electrochemical Oxidation of Fe_2(dobpdc). Encouraged by the results of chemical oxidation suggesting charge mobility, electrochemical oxidation was attempted (Figure 2b). In a three-electrode Swagelok T-cell, a composite of Fe_2(dobpdc) with the conductive carbon Super P (30 wt %) and polyvinylidene difluoride (10 wt %) was dropcast onto a 0.5 in. diameter carbon cloth current collector. Lithium reference and counter electrodes were used to enable comparisons with previously reported materials. Specific capacities were determined from the mass of Fe_2(dobpdc) in the electrode. Figure 4a shows a charge−discharge curve for the composite in a 0.1 M electrolyte solution of lithium tetrafluoroborate in propylene carbonate collected at a rate of C/60. As the material is oxidized, the cell potential rises steadily. This increase is consistent with ex situ powder X-ray diffraction data (Figure 3b), which shows little change in the pattern except for a gradual shift of peaks to higher angles. Again, this results from a gradual contraction of the unit cell, approaching what would be expected for the conversion of iron(II) to iron(III). No new diffraction peaks are apparent, and no significant changes in peak intensities arise. Accordingly, Fe_2(dobpdc)$(BF_4)_x$ ($0 \le x \le 2$) can be considered to be a single phase.

This strong correlation between iron centers is not seen in other microporous iron-based electrodes, such as Prussian blue analogues or ferric metal−organic frameworks,[21,22,25,40,41] nor is it observed for the oxidative intercalation of graphite, where intercalation follows a series of phase changes, known as staging.[42,43] The observation can be attributed to the particularly dense packing of iron centers at the vertices of the honeycomb lattice and the comparatively short distance between neighboring iron sites, as shown in Table S3. This also may be expected given the strong intrachain magnetic coupling reported previously for Fe_2(dobdc).[44]

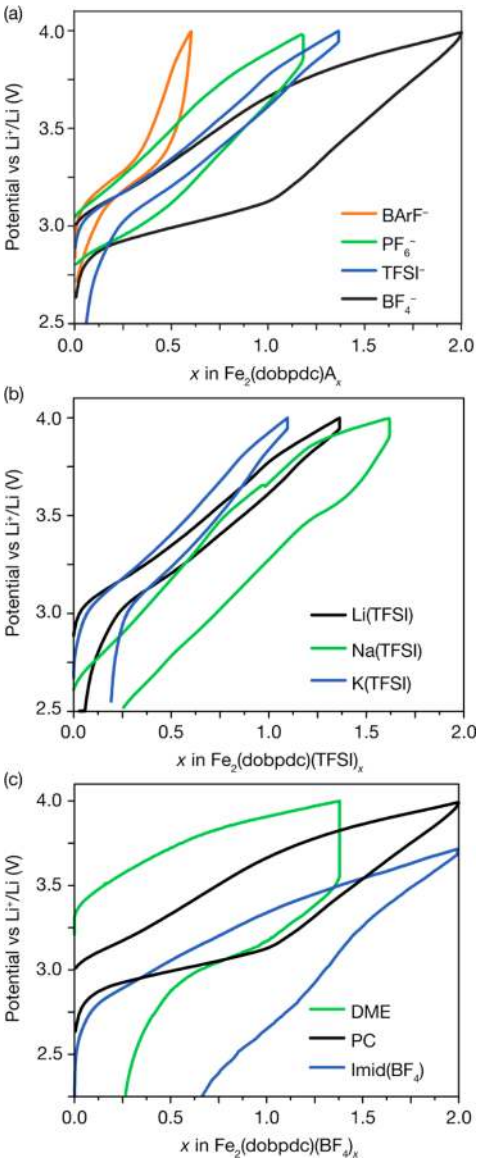

Figure 4. Charge−discharge dependencies on the (a) electrolyte anion, (b) cation, and (c) solvent. All electrolyte solutions were 0.1 M in propylene carbonate (PC) for the anion and cation dependence experiments. In the case of (c) solvent dependence, all solutions contained 0.1 M $LiBF_4$. All data was collected at a rate of C/60.

The ^{57}Fe Mössbauer spectra obtained ex situ for the electrochemically oxidized materials are similar to those obtained for chemically oxidized samples. As shown in Figure 3c and Table S9, discrepancies between the fractional oxidation states determined electrochemically and peak fits of the Mössbauer spectra are smaller than those for the chemically oxidized samples. Additionally, upon charging to an all-ferric state and discharging back to the all-ferrous form, the ferric doublet vanishes completely, and only the original ferrous signal is apparent. This nicely confirms the reversibility of the oxidative electroinsertion reaction.

DOI: 10.1021/jacs.5b08022
J. Am. Chem. Soc. XXXX, XXX, XXX−XXX

The open-circuit potentials for equilibrated samples of $Fe_2(dobpdc)(BF_4)_x$ with $x = 0$ and 2 were observed to be 2.95 and 3.96 V vs Li^+/Li, respectively. The potential of the all-ferric phase is conspicuously high in comparison to that of ferric electrodes of similar structure. This can be attributed to the transformation of a neutral host lattice into a negatively charged lattice, as opposed to the situation for $Fe_2(dobpdc)(BF_4)_x$, in which a cationic framework is reduced to a neutral one. Although the average discharge potential of $Fe_2(dobpdc)(BF_4)_x$ is less than the 3.90 V of iron triplite, this strategy of increasing the redox potential of an iron-based electrode via charge cooperativity in a cationic host presents an alternative to the more general and popular inductive effect.[45] Integration of the discharge curve in Figure 4a yields a specific energy of 415 Wh/kg for $Fe_2(dobpdc)(BF_4)_x$.[46] This is comparable to that of the outstanding lithium-insertion material $LiFePO_4$ (414 Wh/kg) and the graphite-intercalation compound $C_{20}(TFSI)$ (397 Wh/kg).[47,48] Although cycling in this electrolyte came with a small but steady decay in capacity, it is important to note that this is to our knowledge one of the only metal−organic frameworks that demonstrates a competitive specific energy. For the tetrafluoroborate anion in Figure 4a, the charge−discharge cycle is asymmetric, and we suspect that this anion may to some degree displace solvent at the iron center and interact more strongly with the host lattice than initially anticipated.

2.3. Ligand-Centered Redox Activity. In principle, the quinoidal $dobpdc^{4-}$ ligand may be expected to yield a delocalized radical anion upon oxidation to $dobpdc^{\bullet 3-}$; however, this species, present in $Fe_2(dobpdc)A_x$ ($2 < x < 3$), was not cleanly accessible. Electrochemically, a second oxidation process was observed above 4.1 V vs Li/Li^+, but was not reversible. Given the small size of tetrafluoroborate, 78 $Å^3$, the redox activity of the ligand should not be constrained by pore packing.[49] Likely, the diminished lattice enthalpy upon partial oxidation of the ligand renders the transformation irreversible.

The ligand radical itself is, however, clearly observable in the otherwise redox-inactive $Mg_2(dobpdc)$ congener upon chemical oxidation with nitrosonium hexafluorophosphate (Figure 2c). Addition of an acetonitrile solution of this oxidant results in an immediate color change of the solid from white to dark green, together with the evolution of bubbles from the solution. As shown in Figure 3a, the UV−vis−NIR spectrum of the resulting material, $Mg_2(dobpdc)(PF_6)_{0.48}$, displays a new peak at 1.49 eV with a narrower bandwidth than that observed for the $Fe^{II/III}$ intervalence charge-transfer band of $Fe_2(dobpdc)(PF_6)$. This matches nicely with other reported oligophenyl quinone radical anions and is diagnostic of the formation of the semiquinoid radical.[50,51]

By powder X-ray diffraction, a small contraction of just 0.9% in the unit cell volume is observed for $Mg_2(dobpdc)(PF_6)_{0.48}$ (Figure 3e and Table S7). As shown in the structure in Figure 1, the long axis of the biphenyl linker runs nearly parallel to the *a* axis of the unit cell, and the phenoxy−metal bonds lie along neither the *a* axis nor the *c* axis. Upon oxidation, the *a* axis contracts as the bond order increases for the phenolic C−O and C−C bonds, bridging the two phenyl rings. The *c* axis expands very slightly, as would be expected from a weakening of the phenolic Mg−O bonds arising from the less nucleophilic character of the oxidized ligand. In the infrared spectra shown in Figure 3d, a new intense C−O stretch is seen to emerge at 1661 cm^{-1}, consistent with oxidation of the $dobpdc^{4-}$ ligand, as well as a P−F stretch at 827 cm^{-1}, confirming insertion of PF_6^-. Attempts to oxidize $Mg_2(dobpdc)(PF_6)_x$ to the quinone phase ($x = 2$) resulted in amorphous orange powders.

2.4. Electrolyte Dependence. The rigidity of the $Fe_2(dobpdc)$ framework imposes a charge capacity curtailment that becomes more severe with increasing size of the counteranion, as reflected in the data shown in Figure 4a. With a lithium electrolyte solution containing BF_4^- (76 $Å^3$), the material can be oxidized to $x = 2$.[49] The larger $TFSI^-$ (212 $Å^3$) and tetrakis(perfluorophenyl)borate ($BArF^-$, 580 $Å^3$) ions exhibit significantly reduced capacities, $x = 1.36$ and 0.60 equiv, respectively. Interestingly, at 1.18 equiv, PF_6^- (89 $Å^3$) affords a lower charge capacity than $TFSI^-$, despite its much smaller size. This may be the result of coinsertion of neutral $LiPF_6$ or some otherwise convoluted ion pairing of the cation. Voltage hysteresis was smaller for the larger cations, the opposite of what would be expected if electrode polarization was caused by ion diffusivity. Rather, it is more suggestive of voltage polarization being determined by the larger anions having a weaker electrostatic attraction to the cationic iron centers lining the framework channels. This would also explain the significantly higher equilibrium potentials observed for larger cations. A similar phenomenon has been reported for cationic graphite intercalation compounds, wherein larger anions result in significantly higher cell voltages.[8]

To a first approximation, anion insertion materials should not be expected to display a dependence on the nature of the countercation present in the electrolyte solution. The anion $TFSI^-$ was selected for the superior solubility of its Li^+, Na^+, and K^+ salts in propylene carbonate and the reasonably high charge capacity already observed for its Li^+ salt. As shown in Figure 4b, the three salts gave rise to reversible oxidation reactions at similar potentials, and there is no clear trend in charge capacity. However, in a nanoporous electrode like $Fe_2(dobpdc)(TFSI)_x$, the reaction becomes convoluted. Instead of deinsertion of an anion from $Fe_2(dobpdc)(TFSI)_x$ upon discharge (formally the microscopic reverse of the oxidation), a cation could be inserted for charge balance. We have previously found that the isostructural $Mg_2(dobpdc)$ absorbs significant amounts of metal salts even without the driving force of oxidation.[52] The actual insertion mechanism likely involves some combination of these two scenarios. In fact, it is possible that metal−organic frameworks that electroinsert cations may in actuality have a similarly convoluted insertion mechanism.

The electrochemical insertion reaction was found to be more sensitive to solvent than to the inserted salt (Figure 4c). A set of 0.1 M $LiBF_4$ electrolyte solutions were prepared and tested using different solvents. Because every five-coordinate iron(II) center in the evacuated material will become solvated upon introduction of the electrolyte solution, the pore volume is always occupied with more solvent than anions. The effect on cell performance was found to be dramatic. Dimethoxyethane (DME), which is not much larger than propylene carbonate (PC), displayed a massive voltage hysteresis and much reduced capacity. A solution of lithium tetrafluoroborate dissolved in the ionic liquid 1-butyl-3-methyl-imidizolium tetrafluoroborate showed a significantly lower equilibrium potential than for the all-ferrous $Fe_2(dobpdc)$ compound as well as that for the oxidative potential sweep overall. In this electrolyte, the only available nucleophile is the charge-balancing tetrafluoroborate anion, which necessarily coordinates to the iron sites. With an inner sphere counterion, a lower cell potential would be expected. A postmortem analysis of the cell revealed significant

DOI: 10.1021/jacs.5b08022
J. Am. Chem. Soc. XXXX, XXX, XXX−XXX

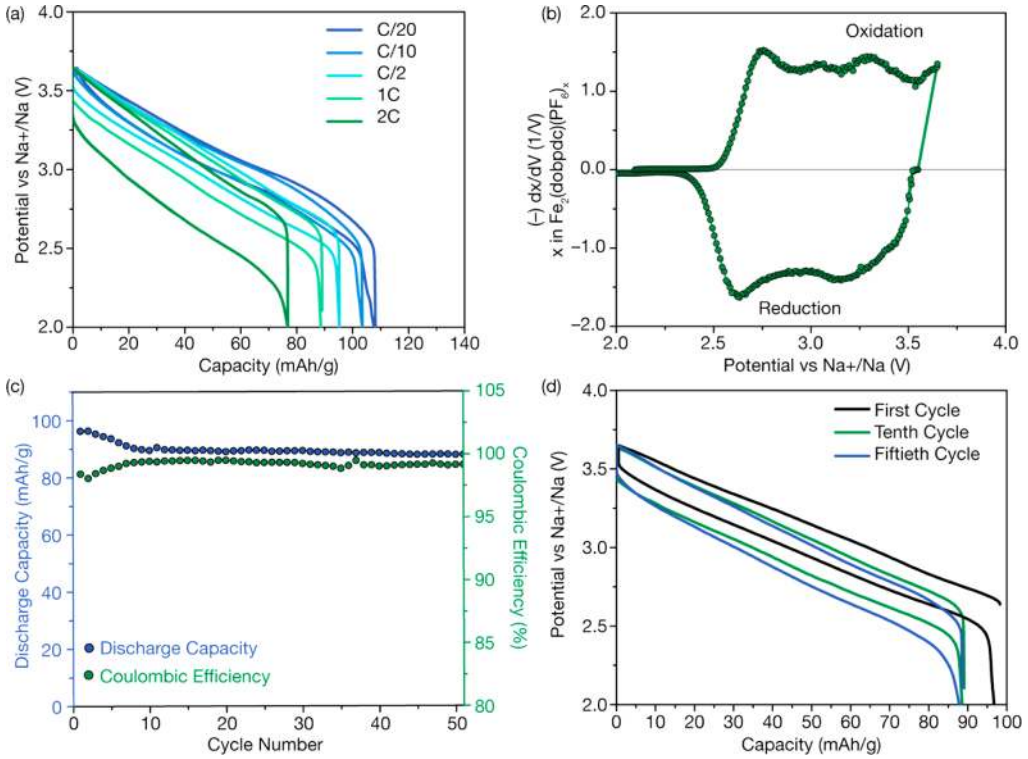

Figure 5. Half-cell performance of a prototype sodium battery with a 0.6 M $NaPF_6$ electrolyte in 30:70 EC/DMC. The theoretical capacity is 140 mAh/g. (a) Cycle rate dependence, (b) differential capacity plot after 49 cycles at 1 C, (c) change in capacity with cycle number at 1 C, and (d) discharge profiles at different points during cycling at 1 C.

electrolyte decomposition at the counter electrode and cycling was not possible. The solvent dependence on the charge–discharge curves for this material is complicated and unintuitive. Indeed, the solvation and conductance of ions in nanoconfined spaces remains a complex and still poorly understood phenomenon, one that electroactive metal–organic frameworks may be excellent candidates for elucidating.[53−56]

2.5. A Sodium Half-Cell. The search for new materials amenable for use in sodium batteries is a burgeoning field. Iron-based and certain organic-based electrode materials are of particular interest here, owing to the potential for reduced material costs and greater elemental abundance.[57] To our knowledge, metal–organic frameworks have not yet been considered for sodium batteries. Given the complex dependence of electrochemical performance with electrolyte and the low-lying quasireversible oxidation of the ligand, it was only after significant optimization that quality cycling conditions were obtained. With a sodium reference electrode, the potential limits were set to 3.65 and 2.00 V. A previously vetted electrolyte consisting of 0.6 M $NaPF_6$ in a 30:70 ethylene carbonate/dimethyl carbonate (EC/DMC) mixture was ultimately found to perform well.[58]

The dependence of the charge/discharge rate upon capacity within the resulting battery construct is shown in Figure 5a. At a rate of C/2, ∼ 170 mV of voltage hysteresis occurs, which is gradually diminished at slower rates. At C/2, ∼ 67% of the iron sites are reversibly oxidized, comparable to what was accessible in $Li_xFe_2(bdc)(OH)_{0.8}F_{0.2}$ at a 40 h discharge rate.[21] From comparison of the two framework structures, it is clear that the much larger pore size and significantly closer iron–iron contacts within $Fe_2(dobpdc)$ are responsible for the faster kinetics. At C/20, the specific energy of the $Fe_2(dobpdc)$ electrode is 316 Wh/kg; however, with such a large pore volume, the energy density is a comparatively modest, 212 Wh/L.

Figure 5b displays the differential capacity as a function of potential versus Na^+/Na for data collected at C/2 after 49 cycles. The oxidative sweep shows three broad peaks and the onset of a fourth tentatively attributed to ligand oxidation. The first peak matches the open-circuit potential of the pristine electrode at 2.75 V. The reductive sweep shows one very broad peak and a second sharper peak at 2.63 V juxtaposed to the initial oxidative peak. Although the Coulombic efficiency of this cycle was greater than 99%, the peak asymmetry suggests that the deinsertion process is different from the insertion process which is possibly a result of changes in ion packing as the concentration of PF_6^- increases or that the asymmetry of the reductive process is convoluted by simultaneous cation insertion and anion deinsertion.

The results from cycling the electrode at 1 C are shown in Figure 5c. After 10 cycles, the cell capacity plateaued at approximately 90 mAh/g, tenuously confirming long-term reversibility of PF_6^- intercalation. Eventually, the material preferentially cycles between $0.58 < x < 1.92$. Previously, we reported ionic conductivity in a similar framework to be most strongly dependent upon the quantity of ions that can be absorbed.[52,59] This observation is in agreement with the preference revealed here toward discharging at higher concentrations of PF_6^-. The change in the discharge profile between the 10th and the 50th cycle is indicative of slower electrode kinetics at high cycle numbers, whereas the total capacity remains the same (Figure 5d).

Figure 6 compares the discharge curve of $Fe_2(dobpdc)(PF_6)_x$ to that of other metal–organic frameworks, sodium-inserting iron phosphates, and $TFSI^-$-intercalated graphite at the slowest discharge rates reported.[21,22,25,60−63] With the exception of

DOI: 10.1021/jacs.5b08022
J. Am. Chem. Soc. XXXX, XXX, XXX–XXX

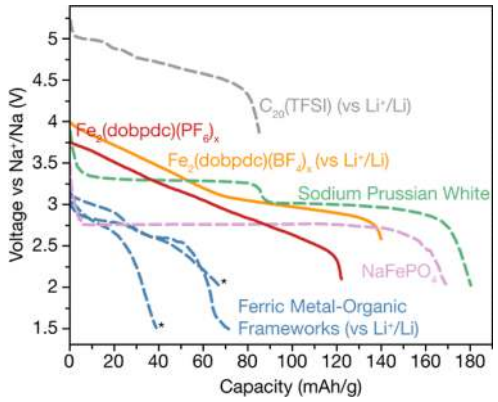

Figure 6. Comparison of $Fe_2(dobpdc)(PF_6)_x$ discharge profile compared to those of other electrodes discharged at their maximum capacity. All materials shown store charge via an $Fe^{II/III}$ couple with the exception of $C_{20}(TFSI)$. Reversible conditions were not reported for the starred curves. Discharge curves measured with a lithium reference were not rescaled.

graphite, all discharge curves plotted also store charge via an $Fe^{II/III}$ couple. This comparison reveals some striking differences for $Fe_2(dobpdc)(PF_6)_x$ ($0.21 < x < 2$). First, its electrode potential decreases almost linearly with reduction, whereas other microporous electrodes, iron phosphate, and graphite show one or multiple plateaus. Second, the strong charge correlation upon charging yields an exceptionally high redox potential, higher than sodium Prussian white for 32% of the discharge. Indeed, the phases $Fe_2(dobpdc)(A)_x$ are unique in possessing very large pores but a high linear density of redox-active metal centers that allow this novel behavior. Finally, in comparison to graphite-intercalation electrodes, the operating potential is much lower. Similar to polymer electrodes, metal–organic frameworks that can insert anions may yield a large range of operating voltages. More broadly, postsynthetic oxidation of a host metal–organic framework, as demonstrated here, opens the door to more exotic electrochemical transformations and applications beyond energy storage.

3. CONCLUSIONS

The metal–organic frameworks $Fe_2(dobdc)$ and $Fe_2(dobpdc)$ were found to oxidatively insert weakly coordinating anions. The reactions proceed both chemically and electrochemically. Upon partial oxidation of $Fe_2(dobpdc)$, the electronic properties of the material changed dramatically, as evidenced by the emergence of a strong intervalence charge-transfer band indicative of enhanced charge mobility. Powder X-ray diffraction, UV–vis spectroscopy, and Coulombic titration all afforded results consistent with classifying $Fe_2(dobpdc)(A)_x$, $0 < x < 2$ as a single phase. Redox activity of the analogous magnesium-based framework confirmed suspicions that a second, quasireversible oxidation at the quinoidal ligand was also accessible. Capacity fade with cycling and discrepancies in the integrated areas of ^{57}Fe Mössbauer spectra at high levels of oxidation are tentatively attributed to this ligand activation. Sodium half-cells were constructed and found to maintain a greater than 99% Faradaic efficiency over 50 oxidation/reduction cycles. The optimized capacity and voltage of this metal–organic framework resulted in an insertion electrode with specific energy more than double that of other iron-based metal–organic frameworks and comparable to that of graphite-intercalation compounds.

4. EXPERIMENTAL SECTION

4.1. Electrochemical Methods. The working electrodes were prepared in a dry, argon-filled glovebox from a composite of the evacuated metal–organic framework (60 wt %), Super P (30 wt %), and PVdF (10 wt %) suspended in THF. The suspension was dispersed with a horn sonicator, and the inklike mixture was dropcast onto carbon cloth (Fuel Cell Earth) and heated to 180 °C for 3 h to remove residual THF. Because of the open metal sites and high surface area of the active material, mass loss was monitored periodically during the activation step in order to confirm full desolvation and to obtain an accurate mass. The electrode was compressed with a hand press and then transferred to the Swagelok union T cell. Masses of active material typically ranged from 15 to 30 mg. The larger masses were required for ex situ iron-57 Mössbauer spectroscopy and powder X-ray diffraction measurements.

Electrochemical data were collected using a Bio-Logic VMP-3 Multipotentiostat/Galvanostat. All measurements were conducted inside a dry, argon-filled glovebox. Following cell assembly, the cell was left to relax until dV/dt dropped below 0.1 mV/h. Reported open-circuit potentials were determined under the same limiting condition. Measurements reported were all collected under constant current conditions with potential and capacity limitations. All reported data had an oxidative capacity limitation of two equivalents as estimated from the mass of the evacuated framework. Over-reduction was not observed within the lower potential limits that were set.

4.2. Diffuse Reflectance UV–Visible–NIR Spectroscopy. Samples were prepared in a dry, argon-filled glovebox by diluting the pure samples in PVdF (background subtracted). The sample was pelletized in a custom-built airtight cell with quartz windows and sealed. Spectra were collected on a Cary 5000 by Varian spectrophotometer equipped with a reflectance sphere.

4.3. FT-IR Spectroscopy. Air- and water-free spectra were collected on a PerkinElmer Spectrum-400 FT-IR with an attenuated total reflectance accessory (Pike Technologies GladiATR) and equipped with a home-built, dry nitrogen-filled glovebag attachement.

4.3. Iron-57 Mössbauer Spectroscopy. Mössbauer spectra were collected at 100 K with a constant acceleration spectrometer and a rhodium matrix cobalt-57 source. The instrument was calibrated at 295 K with α-iron foil. The absorbers were composite electrodes (about 30 mg of active material) with a carbon-cloth backing. Chemically oxidized sample contained a similar amount of sample mixed with boron nitride. All samples were prepared and sealed in an argon glovebox.

4.4. Powder X-ray Diffraction. Diffraction data was collected on a Bruker D8 Advance diffractometer using Cu Kα (λ = 1.5406 Å) radiation. All data reported were collected inside 1 mm diameter glass capillaries with 0.01 mm thick walls (Charles Supper). Capillaries were packed inside a dry, argon-filled glovebox and then flame-sealed. Some data shows a weak, very broad feature that tapers off above 20° that originates from the glass capillary. Unit cells were determined by Le Bail refinment using the software package Topas (Bruker).

4.5. Chemical Oxidation of Fe_2(2,5-dihydroxybenzene-1,4-dicarboxylate). $Fe_2(dobdc)$ and thianthrenium hexafluorophosphate ($C_{12}H_8S_2^{\bullet+}PF_6^-$) were both prepared by previously reported procedures.[28,64] In a dry, argon-filled glovebox, 24.3 mg (0.0795 mmol) of $Fe_2(dobdc)$ was suspended in MeCN (~6 mL) and stirred virgorously in a 20 mL glass scintillation vial. In another vial, 28.7 mg (0.0794 mmol) of $C_{12}H_8S_2^{\bullet+}PF_6^-$ was dissolved in ~4 mL of MeCN. To the stirring suspension, $Th^{\bullet+}PF_6^-$ was added dropwise. The vial was sealed and left to stir at room temperature for ~16 h. The black suspension was filtered to recover a free-flowing powder. Unit cell refinement and ^{57}Fe Mössbauer spectra with fits are reported in the Supporting Information. The chemical formula estimated from ^{57}FeMossbauer and the observed unit cell contraction is $Fe_2(dobdc)(PF_6)_{0.96}\cdot x$MeCN.

4.6. Synthesis of Fe_2(4,4′-dioxidobiphenyl-3,3′-dicarboxylate)$(PF_6)_{0.84}\cdot$~5.1MeCN. The compound $Fe_2(dobpdc)$ was prepared as previously reported.[36] In a dry, argon-filled glovebox, 22.9 mg (0.0600 mmol) of $Fe_2(dobpdc)$ was suspended in ~6 mL of

DOI: 10.1021/jacs.5b08022
J. Am. Chem. Soc. XXXX, XXX, XXX–XXX

acetonitrile and stirred vigorously in a 20 mL glass scintillation vial. In another vial, 21.7 mg (0.0601 mmol) of $C_{12}H_8S_2^{\bullet+}PF_6^-$ was dissolved in ~4 mL of acetonitrile. To the stirring suspension, $C_{12}H_8S_2^{\bullet+}PF_6^-$ was added dropwise. The vial was sealed and left to stir at room temperature for ~16 h. The black suspension was filtered to recover a free-flowing powder. Unit cell refinements and ^{57}Fe Mössbauer spectra with fits are reported in the Supporting Information. Infrared (solid ATR) spectroscopy: 1654 (m), 1611 (s), 1547 (s), 1529 (s), 1462 (s), 1408 (s), 1371 (m), 1280 (m), 1226 (s), 1153 (m), 1104 (m), 1052 (m), 884 (m), 840 (s), 826 (s), 805 (s), 690 (s), 621 (m), 592 (s).

4.7. Synthesis of Fe_2(dobpdc)$(PF_6)_{1.56}$·~5.1MeCN. In a dry, argon-filled glovebox, 13.8 mg (0.0361 mmol) of Fe_2(dobpdc) was suspended in ~6 mL of acetonitrile and stirred vigorously in a 20 mL glass scintillation vial. In another vial, 26.0 mg (0.0719 mmol) of $C_{12}H_8S_2^{\bullet+}PF_6^-$ was dissolved in ~4 mL of MeCN. To the stirring suspension, $C_{12}H_8S_2^{\bullet+}PF_6^-$ was added dropwise. The vial was sealed and left to stir at room temperature for ~16 h. The black suspension was filtered to recover a free-flowing powder. The molecular formula was estimated from ^{57}Fe Mossbauer and the observed unit cell contraction. Infrared (solid ATR) spectroscopy: 1652 (m), 1610 (s), 1547 (s), 1523 (s), 1462 (s), 1406 (s), 1362 (m), 1280 (m), 1224 (m), 1154 (m), 1104 (m), 1052 (m), 884 (m), 839 (s), 805 (m), 691 (s), 621 (m), 593 (s).

4.8. Synthesis of Mg_2(dobpdc)$(PF_6)_{0.48}$·5.1MeCN. Mg_2(dobpdc) was prepared as previously reported.[36] In a dry, argon-filled glovebox, 50 mg (0.16 mmol) of Mg_2(dobpdc) was suspended in ~6 mL of acetonitrile and stirred vigorously in a 20 mL glass scintillation vial. In another vial, 27 mg (0.16 mmol) of $NOPF_6$ (Aldrich) was dissolved in ~4 mL of acetonitrile. To the stirring suspension, $NOPF_6$ was added dropwise. The powder turned from white to dark green immediately. The vial was sealed and left to stir at room temperature for ~16 h. The dark-green suspension was filtered to recover a free-flowing powder. Analytical: $Mg_2(C_{14}H_6O_6)(PF_6)_{0.48}(C_2H_3N)_{5.1}$ calculated: C, 48.6, H, 3.59, N, 11.95; found: C, 48.63, H, 3.72, N, 11.93. Infrared (solid ATR) spectroscopy: 1661 (s), 1564 (s), 1573 (s), 1467 (s), 1448 (s), 1424 (s), 1291 (m), 1941 (s), 909 (m), 886 (m), 827 (s), 686 (m), 591 (m).

■ ASSOCIATED CONTENT

Supporting Information

The Supporting Information is available free of charge on the ACS Publications website at DOI: 10.1021/jacs.5b08022.

Additional details with regards to experimental methods, unit cell refinments, Mössbauer analysis, absorption edge analysis, calculation of ion sizes, iron distances, and discharge curves from the literature (PDF)

■ AUTHOR INFORMATION

Corresponding Author

*E-mail: jrlong@berkeley.edu.

Funding

This research was supported by the National Science Foundation under award no. DMR-1309066. We would also like to thank Arkema for fellowship support of M.L.A.

Notes

The authors declare no competing financial interest.

■ REFERENCES

(1) Jacobson, A. J.; Nazar, L. F. Intercalation Chemistry. In *Encyclopedia of Inorganic and Bioinorganic Chemistry*; John Wiley & Sons: Hoboken, NJ, 2011; pp 1−37.

(2) Huggins, R. A. *Solid State Ionics* **1998**, *113-115*, 533−544.

(3) Besenhard, J. O.; Fritz, H. P. *Angew. Chem., Int. Ed. Engl.* **1983**, *22*, 950−975.

(4) Khan, A. I.; O'Hare, D. *J. Mater. Chem.* **2002**, *12*, 3191−3198.

(5) He, J.; Wei, M.; Li, B.; Kang, Y.; Evans, D. G.; Duan, X. *Struct. Bonding (Berlin)* **2006**, *119*, 89−118.

(6) Goh, K. H.; Lim, T. T.; Dong, Z. *Water Res.* **2008**, *42*, 1343−1368.

(7) Nakano, H.; Sugiyama, Y.; Morishita, T.; Spencer, M. J. S.; Snook, I. K.; Kumai, Y.; Okamoto, H. *J. Mater. Chem. A* **2014**, *2*, 7588−7592.

(8) Katinonkul, W.; Lerner, M. M. *J. Fluorine Chem.* **2007**, *128*, 332−335.

(9) Novak, P.; Muller, K.; Santhanam, K. S. V.; Haas, O. *Chem. Rev.* **1997**, *97*, 207−281.

(10) Baughman, R. H. *Synth. Met.* **1996**, *78*, 339−353.

(11) Smela, E. *Adv. Mater.* **2003**, *15*, 481−494.

(12) Zhou, H. C.; Kitagawa, S. *Chem. Soc. Rev.* **2014**, *43*, 5415−5418.

(13) Long, J. R.; Yaghi, O. M. *Chem. Soc. Rev.* **2009**, *38*, 1213−1214.

(14) Tanabe, K. K.; Cohen, S. M. *Chem. Soc. Rev.* **2011**, *40*, 498−519.

(15) Wang, Z. Q.; Cohen, S. M. *Chem. Soc. Rev.* **2009**, *38*, 1315−1329.

(16) Talin, A. A.; Centrone, A.; Ford, A. C.; Foster, M. E.; Stavila, V.; Haney, P.; Kinney, R. A.; Szalai, V.; El Gabaly, F.; Yoon, H. P.; Léonard, F.; Allendorf, M. D. *Science* **2014**, *343*, 66−69.

(17) Park, S. S.; Hontz, E. R.; Sun, L.; Hendon, C. H.; Walsh, A.; Van Voorhis, T.; Dincă, M. *J. Am. Chem. Soc.* **2015**, *137*, 1774−1777.

(18) Sheberla, D.; Sun, L.; Blood-Forsythe, M. A.; Er, S. l.; Wade, C. R.; Brozek, C. K.; Aspuru-Guzik, A. N.; Dincă, M. *J. Am. Chem. Soc.* **2014**, *136*, 8859−8862.

(19) Hmadeh, M.; Lu, Z.; Liu, Z.; Gándara, F.; Furukawa, H.; Wan, S.; Augustyn, V.; Chang, R.; Liao, L.; Zhou, F.; et al. *Chem. Mater.* **2012**, *24*, 3511−3513.

(20) Kaveevivitchai, W.; Jacobson, A. J. *J. Power Sources* **2015**, *278*, 265−273.

(21) Ferey, G.; Millange, F.; Morcrette, M.; Serre, C.; Doublet, M. L.; Greneche, J. M.; Tarascon, J. M. *Angew. Chem., Int. Ed.* **2007**, *46*, 3259−3263.

(22) Fateeva, A.; Horcajada, P.; Devic, T.; Serre, C.; Marrot, J.; Greneche, J. M.; Morcrette, M.; Tarascon, J. M.; Maurin, G.; Ferey, G. *Eur. J. Inorg. Chem.* **2010**, *2010*, 3789−3794.

(23) Meilikhov, M.; Yusenko, K.; Torrisi, A.; Jee, B.; Mellot-Draznieks, C.; Pöppl, A.; Fischer, R. A. *Angew. Chem., Int. Ed.* **2010**, *49*, 6212−6215.

(24) Zhang, Z. Y.; Yoshikawa, H.; Awaga, K. *J. Am. Chem. Soc.* **2014**, *136*, 16112−16115.

(25) Shin, J.; Kim, M.; Cirera, J.; Chen, S.; Halder, G. J.; Yersak, T. A.; Paesani, F.; Cohen, S. M.; Meng, Y. S. *J. Mater. Chem. A* **2015**, *3*, 4738−4744.

(26) Morozan, A.; Jaouen, F. *Energy Environ. Sci.* **2012**, *5*, 9269−9290.

(27) Bredas, J. L.; Street, G. B. *Acc. Chem. Res.* **1985**, *18*, 309−315.

(28) Bloch, E. D.; Murray, L. J.; Queen, W. L.; Chavan, S.; Maximoff, S. N.; Bigi, J. P.; Krishna, R.; Peterson, V. K.; Grandjean, F.; Long, G. J.; Smit, B.; Bordiga, S.; Brown, C. M.; Long, J. R. *J. Am. Chem. Soc.* **2011**, *133*, 14814−14822.

(29) Caskey, S. R.; Wong-Foy, A. G.; Matzger, A. J. *J. Am. Chem. Soc.* **2008**, *130*, 10870−10871.

(30) Rosi, N. L.; Kim, J.; Eddaoudi, M.; Chen, B. L.; O'Keeffe, M.; Yaghi, O. M. *J. Am. Chem. Soc.* **2005**, *127*, 1504−1518.

(31) Sanz, R.; Martinez, F.; Orcajo, G.; Wojtas, L.; Briones, D. *Dalton Trans.* **2013**, *42*, 2392−2398.

(32) Zhou, W.; Wu, H.; Yildirim, T. *J. Am. Chem. Soc.* **2008**, *130*, 15268−15269.

(33) Sun, L.; Hendon, C. H.; Minier, M. A.; Walsh, A.; Dincă, M. *J. Am. Chem. Soc.* **2015**, *137*, 6164−6167.

(34) Cozzolino, A. F.; Brozek, C. K.; Palmer, R. D.; Yano, J.; Li, M.; Dincă, M. *J. Am. Chem. Soc.* **2014**, *136*, 3334−3337.

(35) Deng, H. X.; Grunder, S.; Cordova, K. E.; Valente, C.; Furukawa, H.; Hmadeh, M.; Gandara, F.; Whalley, A. C.; Liu, Z.; Asahina, S.; Kazumori, H.; O'Keeffe, M.; Terasaki, O.; Stoddart, J. F.; Yaghi, O. M. *Science* **2012**, *336*, 1018−1023.

DOI: 10.1021/jacs.5b08022
J. Am. Chem. Soc. XXXX, XXX, XXX−XXX

(36) McDonald, T. M.; Mason, J. A.; Kong, X.; Bloch, E. D.; Gygi, D.; Dani, A.; Crocellà, V.; Giordanino, F.; Odoh, S. O.; Drisdell, W. S.; et al. *Nature* **2015**, *519*, 303−308.
(37) Robin, M. B.; Day, P. *Adv. Inorg. Chem. Radiochem.* **1968**, *10*, 247−422.
(38) Burns, R. G. *Annu. Rev. Earth Planet. Sci.* **1981**, *9*, 345−383.
(39) Feller, R. K.; Cheetham, A. K. *Solid State Sci.* **2006**, *8*, 1121−1125.
(40) Wang, R. Y.; Shyam, B.; Stone, K. H.; Weker, J. N.; Pasta, M.; Lee, H.-W.; Toney, M. F.; Cui, Y. *Adv. Energy Mater.* **2015**, *5*, 1401869.
(41) Lu, Y.; Wang, L.; Cheng, J.; Goodenough, J. B. *Chem. Commun.* **2012**, *48*, 6544−6546.
(42) Jobert, A.; Touzain, P.; Bonnetain, L. *Carbon* **1981**, *19*, 193−198.
(43) Seel, J. A.; Dahn, J. R. *J. Electrochem. Soc.* **2000**, *147*, 892−898.
(44) Maurice, R.; Verma, P.; Zadrozny, J. M.; Luo, S. J.; Borycz, J.; Long, J. R.; Truhlar, D. G.; Gagliardi, L. *Inorg. Chem.* **2013**, *52*, 9379−9389.
(45) Barpanda, P.; Ati, M.; Melot, B. C.; Rousse, G.; Chotard, J. N.; Doublet, M. L.; Sougrati, M. T.; Corr, S. A.; Jumas, J. C.; Tarascon, J. M. *Nat. Mater.* **2011**, *10*, 772−779.
(46) Given the large number of anions and fluctuations in solvation states for the compounds reported herein, all charge capacities were calculated using the mass of host lattice only in order to make chemically meaningful comparisons. Because this diverges from normal convention, all literature values reported here were recalculated from the original discharge curves using the mass of the host lattice and not the mass of the reactants in the electrochemical reaction.
(47) Placke, T.; Bieker, P.; Lux, S. F.; Fromm, O.; Meyer, H.-W.; Passerini, S.; Winter, M. *Z. Phys. Chem.* **2012**, *226*, 391−407.
(48) Padhi, A. K.; Nanjundaswamy, K. S.; Goodenough, J. B. *J. Electrochem. Soc.* **1997**, *144*, 1188−1194.
(49) Volumes of anions were estimated from the cell volumes of their lithium salts. These values are tabulated with citations in the Supporting Information.
(50) Nelsen, S. F.; Weaver, M. N.; Telo, J. P. *J. Phys. Chem. A* **2007**, *111*, 10993−10997.
(51) Hankache, J.; Wenger, O. S. *Chem. Rev.* **2011**, *111*, 5138−5178.
(52) Aubrey, M. L.; Ameloot, R.; Wiers, B. M.; Long, J. R. *Energy Environ. Sci.* **2014**, *7*, 667−671.
(53) Wang, H.; Forse, A. C.; Griffin, J. M.; Trease, N. M.; Trognko, L.; Taberna, P.-L.; Simon, P.; Grey, C. P. *J. Am. Chem. Soc.* **2013**, *135*, 18968−18980.
(54) Fornasiero, F.; Park, H. G.; Holt, J. K.; Stadermann, M.; Grigoropoulos, C. P.; Noy, A.; Bakajin, O. *Proc. Natl. Acad. Sci. U. S. A.* **2008**, *105*, 17250−17255.
(55) Liu, L.; Chen, X.; Lu, W. Y.; Han, A. J.; Qiao, Y. *Phys. Rev. Lett.* **2009**, *102*, 184501.
(56) Zwolak, M.; Lagerqvist, J.; Di Ventra, M. *Phys. Rev. Lett.* **2009**, *103*, 128102.
(57) Larcher, D.; Tarascon, J. M. *Nat. Chem.* **2014**, *7*, 19−29.
(58) Bhide, A.; Hofmann, J.; Durr, A. K.; Janek, J.; Adelhelm, P. *Phys. Chem. Chem. Phys.* **2014**, *16*, 1987−1998.
(59) Wiers, B. M.; Foo, M. L.; Balsara, N. P.; Long, J. R. *J. Am. Chem. Soc.* **2011**, *133*, 14522−14525.
(60) Individual discharge curves are labeled in the Supporting Information with the specific phase transformation and corresponding citation.
(61) Wang, L.; Song, J.; Qiao, R.; Wray, L. A.; Hossain, M. A.; Chuang, Y.-D.; Yang, W.; Lu, Y.; Evans, D.; Lee, J.-J.; Vail, S.; Zhao, X.; Nishijima, M.; Kakimoto, S.; Goodenough, J. B. *J. Am. Chem. Soc.* **2015**, *137*, 2548−2554.
(62) Oh, S.-M.; Myung, S.-T.; Hassoun, J.; Scrosati, B.; Sun, Y.-K. *Electrochem. Commun.* **2012**, *22*, 149−152.
(63) Placke, T.; Rothermel, S.; Fromm, O.; Meister, P.; Lux, S. F.; Huesker, J.; Meyer, H.-W.; Winter, M. *J. Electrochem. Soc.* **2013**, *160*, A1979−A1991.
(64) Boduszek, B.; Shine, H. J. *J. Org. Chem.* **1988**, *53*, 5142−5143.

DOI: 10.1021/jacs.5b08022
J. Am. Chem. Soc. XXXX, XXX, XXX−XXX